Journal of Materials Chemistry A

ROYAL SOCIETY OF CHEMISTRY

PAPER

View Article Online
View Journal | View Issue

Cite this: J. Mater. Chem. A, 2022, 10, 13467

Understanding the effect of lattice polarisability on the electrochemical properties of lithium tetrahaloaluminates, $LiAlX_4$ (X = Cl, Br, I)†

Nicolás Flores-González, [a] Martí López, [b] Nicolò Minafra,[c] Jan Bohnenberger,[e] Francesc Viñes, [b] Svemir Rudić, [d] Ingo Krossing,[e] Wolfgang G. Zeier, [c] Francesc Illas [b] and Duncan H. Gregory *[a]

Establishing links between the structure and physical properties of solid-state ionic conductors contributes not only to a rationale of their fundamental nature, but also provides design principles to accelerate the discovery of new materials. Lithium ion conduction in complex halides is not well-elucidated and so the interplay between lattice dynamics, electronic structure, and electrochemical properties in such halides has been explored in the isostructural family of lithium tetrahaloaluminates $LiAlX_4$ (X = Cl, Br, I). Using a combination of experimental methods (diffuse reflectance UV-Vis spectroscopy, pulse-echo speed of sound measurements, Raman spectroscopy, inelastic neutron scattering) and periodic Density Functional Theory (DFT) based calculations, we demonstrate that softer lattices (quantified in terms of Debye frequencies or Li-phonon band centres as a function of X) provide lower activation energies for Li^+ migration. However, the relationship between polarisability and Li^+ conductivity is not straightforward. In line with expectations emergent from the Meyer–Neldel rule, the activation energy for Li^+ hopping, E_a, and the pre-exponential terms collated as σ_0 in the Arrenhius equation for activated conductivity, correlate. It is also evident that the electrochemical oxidative potential limit correlates with the X^- phonon band centre in the Vibrational Density of States (VDOS) and that the Electrochemical stability Window (EW) and optical band gap are interlinked, as expected.

Received 7th April 2022
Accepted 30th May 2022

DOI: 10.1039/d2ta02821b

rsc.li/materials-a

Introduction

Inorganic solid-state electrolytes (SSEs) can be employed in a number of emerging technologies ranging from solid oxide fuel cells to solid-state batteries.[1] In particular, the replacement of flammable liquid electrolytes in conventional Li-ion batteries (LIBs) with solid-state analogues could not only improve their safety and longevity, but also enable higher energy density cells (using Li–metal anodes and high-voltage cathodes) in all-solid batteries (SSBs).[2] During the past four decades, a vast amount of lithium SSEs have been studied. Among them, sulfide-based materials have shown the highest ionic conductivities at room temperature, *e.g.* $Li_{9.54}Si_{1.74}P_{1.44}S_{11.47}Cl_{0.3}$ (σ = 25 mS cm^{-1} for a sintered pellet of 90% density),[3] however their narrow electrochemical windows (*e.g.* 1.7–2.4 and 1.1–2.8 V *vs.* Li^+/Li for the thio-LISICON $Li_{10}GeP_2S_{12}$ and the argyrodite Li_6PS_5Cl, respectively)[4,5] and limited chemical stability have prevented their large-scale commercialization.[4] Among the alternatives, lithium ternary halides, $LiAlX_4$ (X = halogen),[6] Li_xScCl_{3+x},[7] $Li_2Sc_{2/3}Cl_4$,[8] $Li_2In_xSc_{2/3-x}Cl_4$,[9] Li_2ZrCl_6,[10] $Li_3M^{III}X_6$ (M^{III} = Sc, Y, In, La, Ho, Er; X = halogen)[11–17] and $Li_{3-x}M_{1-x}Zr_xCl_6$ (M^{III} = Y, Er),[18] are raising interest with appreciable ionic conductivity at room temperature, low activation energies for Li^+ migration and wide electrochemical windows (*e.g.* 1.75–4.25 and 0.62–4.21 V *vs.* Li^+/Li for Li_2ZrCl_6 and Li_3YCl_6, respectively).[14,19] Despite the fact that most of the ternary halides described above react with water or are highly hygroscopic/deliquescent, recent reports have demonstrated notable exceptions in Li_3InCl_6 and Li_2ZrCl_6.[15,19] While the former chloride will convert to $Li_3InCl_6 \cdot 2H_2O$ when exposed to a humid atmosphere (which can be easily dehydrated by heating under vacuum), the latter showed no signs of moisture uptake nor conductivity degradation after exposure to an atmosphere with 5% relative humidity. Furthermore, it has been shown that the intrinsic instability of

[a]WestCHEM, School of Chemistry, University of Glasgow, Joseph Black Building, Glasgow G12 8QQ, UK. E-mail: Duncan.Gregory@Glasgow.ac.uk

[b]Departament de Ciència de Materials i Química Física & Institut de Química Teòrica i Computacional (IQTCUB), Universitat de Barcelona, C/Martí i Franquès 1, 08028 Barcelona, Spain

[c]Institute for Inorganic and Analytical Chemistry, University of Münster, Correnstr. 39, 48149, Germany

[d]ISIS Pulsed Neutron and Muon Source, STFC Rutherford Appleton Laboratory, Didcot, Oxfordshire, OX11 0QX, UK

[e]Institut für Anorganische und Analytische Chemie and Freiburger Materialforschungszentrum (FMF), Universität Freiburg, Albertstr. 21, 79104 Freiburg, Germany

† Electronic supplementary information (ESI) available. See https://doi.org/10.1039/d2ta02821b

halide SSEs against Li can be overcome by using a InLi alloy or by protecting the electrolyte with a $Li_7P_3S_{11}$ layer.[11,19]

Generally, it can be demonstrated that the ionic conductivity of an electrolyte is given by:[20]

$$\sigma = \left[\frac{\gamma c v_0 a_0^2 (Ze)^2}{k_B T}\right] \exp\left(\frac{\Delta S_m}{k_B}\right) \exp\left(-\frac{\Delta H_m}{k_B T}\right), \quad (1)$$

where γ is a geometric factor that represents the dimensionality of the conduction pathways; c is the carrier density; ν_0 is the attempt frequency, which is the optical-mode vibrational frequency for the mobile ion within its lattice site;[21] a_0 is the jump distance; Z is the charge number of the mobile ion; e is the elementary charge; ΔS_m and ΔH_m are the entropy and enthalpy of migration, respectively; k_B is the Boltzmann constant; and T is the absolute temperature. Eqn (1) can be simplified to give the well-known Arrhenius-like equation for ionic conductivity:

$$\sigma T = \sigma_0 \exp\left(-\frac{E_a}{k_B T}\right), \quad (2)$$

where

$$\sigma_0 = \left[\frac{\gamma c v_0 a_0^2 (Ze)^2}{k_B}\right] \exp\left(\frac{\Delta S_m}{k_B}\right), \quad (3)$$

The activation energy for migration, E_a, depends on the conduction mechanism. For a temperature-independent mobile-ion site occupancy $E_a = \Delta H_m$; for Schottky defects $E_a = \Delta H_m + 1/2\Delta H_S$; and for Frenkel defects $E_a = \Delta H_m + 1/2\Delta H_F$ (ΔH_S and ΔH_F are the enthalpies of formation of Schottky and Frenkel defects, respectively). Steered by eqn (1), design principles and descriptors have been presented in the literature for significant cationic conductivity to occur in a solid. These are typically: (i) a large carrier concentration; (ii) empty and occupied sites with similar potential energies, with a low activation barrier for direct ion hopping between them (*via* channels to allow long range transport, neglecting high-energy transition states); (iii) structural disorder in the cation (or anion) sublattice (as appropriate); (iv) anion (cation) sublattices with *bcc*-like frameworks (as opposed to *ccp* or *hcp* frameworks) to allow cations (anions) to migrate *via* interconnected tetrahedral sites with equivalent energies; and (v) a highly polarisable anion framework (in a cation conductor).[1,22–26] Besides the structural considerations (i–iv), the role of lattice polarisability embodied in (v) (as the underlying cause of lattice softness) and its effect on ionic transport has attracted renewed scrutiny recently.[27,28] It has been hypothesised that increasing the polarisability of anions within isostructural cation conductors (where the conductions pathways do not change significantly) would decrease the activation energy for cation migration. This is based on the idea that decreasing the bond strength between the mobile cation and the anion sublattice (by increasing bond polarity), should lower the migration barrier (since less energy is needed to jump from a stable lattice site). However, research shows that increasing the lattice softness can also decrease the Arrhenius pre-exponential factor (σ_0) by decreasing the corresponding attempt frequency (ν_0), *i.e.* reducing the probability for a Li^+ ion to jump to a neighbouring site, and the entropy of migration (ΔS_m) (eqn (1)).[29,30] These effects will have a competing impact on the ionic conductivity and establishing which might dominate in any given system remains to be determined in the majority of cases. In terms of the quantification of lattice softness, Zeier, Muy and co-workers demonstrated that both acoustic modes (probed by speed of sound measurements) and phonon band centres (as determined by inelastic neutron scattering and density functional theory calculations), may be used as descriptors for the softness of the lattice.[31] However, such studies remain narrow in focus, dealing only with a few families of Li^+ conductors, including argyrodites Li_6PS_5X (X = Cl, Br, I),[27] LISICON materials derived from Li_3PO_4,[32] and NASICON-type $Li_{1-3x}Ga_xZr_2(PO_4)_3$.[30]

Since very little is known about the influence of anion sublattice polarisability on the properties of ternary lithium halides,[13] we focused on the isostructural family of lithium tetrahaloaluminates $LiAlX_4$ (X = Cl, Br, I), using a combination of experimental (DR-UV-Vis, PE-SoS, Raman, and INS) and periodic Density Functional Theory (DFT) based calculations to establish connections between electronic structure, lattice dynamics and electrochemical/transport data to piece together the appropriate composition–structure–property relationships.

Experimental

Synthesis of $LiAlX_4$

LiCl (Sigma Aldrich, ≥99.99%), $AlCl_3$ (Sigma Aldrich, anhydrous, 99.999%), LiBr (Alfa Aesar, anhydrous, 99.995%), $AlBr_3$ (Sigma Aldrich, anhydrous, 99.999%), LiI (Sigma Aldrich, anhydrous, 99.99%) and AlI_3 (Sigma Aldrich, anhydrous, 99.999%) were used as starting materials without further purification. Because of the air and/or moisture sensitivity of the starting materials and the final products, all manipulations were carried out in a continuously purified, Ar-filled (BOC, 99.998%) glove box (MBraun LABstar, $O_2 \leq 5$ ppm, $H_2O \leq 0.5$ ppm). A total of *ca.* 0.5 g of the starting materials were weighed out in the desired molar ratio (1 : 1) and added to a stainless-steel grinding jar containing ten stainless steel balls (10 mm diameter), each of which weighed *ca.* 4 g (giving a Ball-to-Powder Ratio (BPR) of 80 : 1). The grinding jar was sealed under Ar in the glove box before transfer to the ball mill. Ball milling was conducted in a planetary ball mill (Retsch PM100) in 5 minute milling periods (reverse rotation at 450 rpm, 300 rpm and 200 rpm for X = Cl, Br and I, respectively), followed by 5 minute rest periods for durations of 3 h (X = Cl) or 6 h (X = Br, I).[6]

Characterisation

Powder X-ray diffraction

Powder X-ray Diffraction (PXD) measurements were conducted to confirm the identity and purity of mechanochemically-synthesised lithium haloaluminates. PXD data were recorded at room temperature with a Bruker D8 Advance diffractometer in transmission geometry using Cu Kα radiation (1.54184 Å) with a slit size of 2.0 mm. The moisture/air-sensitive samples

were loaded inside glass capillaries (0.5 or 0.7 mm internal diameter), sealed with vacuum grease inside an Ar-filled glovebox, and subsequently flame-sealed outside the glovebox. The aligned capillaries were continuously rotated throughout the analysis and scanned over $5 \leq 2\theta/^\circ \leq 110$ ranges (0.0167 step size, 14–15 h). Collected PXD patterns, as compared to reference data,[6] are presented in the ESI (Fig. S1†) and showed the formation of the desired products without evident impurities.

Electrochemical impedance spectroscopy

Electrical conductivities were measured by AC Electrochemical Impedance Spectroscopy (EIS) using isostatically pressed pellets (325 MPa, measured densities were 88, 84 and 80% of the crystallographically determined values for X = Cl, Br, I, respectively), which were subsequently coated *via* thermal evaporation with thin gold (200 nm) electrodes. Electrochemical impedance analysis was conducted in the temperature range of −40 to 60 °C using a SP300 impedance analyser (Biologic) at frequencies from 7 MHz to 50 mHz with an amplitude of 10 mV. The total ionic conductivities were obtained by fitting the spectra with an equivalent circuit consisting of one (X = Cl) or two (X = Br, I) parallel Constant Phase Element (CPE)/resistor in series with a CPE representing the behaviour of the electrolyte and blocking electrodes, respectively (ESI, Table S8†).[6]

Raman spectroscopy

Raman spectra were recorded at room temperature with a Bruker VERTEX 70 spectrometer equipped with a Bruker RAM II module (1064 nm laser) with a nitrogen-cooled Ge detector. The samples were contained in sealed soda-lime glass Pasteur pipettes and measured over a region of 4000–50 cm^{-1} with a resolution of 4 cm^{-1}.

Inelastic neutron scattering

The experimental Vibrational phonon Density of States (VDOS) for each halide was determined from Inelastic Neutron Scattering (INS) data measured using the TOSCA[33] spectrometer at the ISIS neutron and muon source at the Rutherford Appleton Laboratory in Oxfordshire. Samples (*ca.* 1.5 g) were loaded into aluminium cans and sealed with an indium wire gasket inside an Ar-filled glovebox. INS spectra were recorded at 10 K. Since the non-halide elements in $LiAlX_4$ have small coherent neutron scattering cross sections, samples were scanned for a duration of 2000 μA h (corresponding to ∼12 h of exposure). The empty aluminium cans were measured in identical conditions and these recorded data were subtracted from the sample spectra. INS data were analysed using the Mantid[34] open source software.

Pulse-echo speed of sounds measurements

Pulse-Echo Speed of Sound (PE-SoS) measurements were performed on consolidated discs using an Epoch 600 instrument (Olympus) with 5 MHz transducers for longitudinal and transverse speeds of sound. Measurements were conducted on isostatically pressed pellets (325 MPa) under N_2 atmosphere (O_2 < 40 ppm). In order to prevent side reactions of the couplant and sample, pellets were coated with a thin layer (*ca.* 200 nm) of gold *via* thermal evaporation prior to the measurements. The extraction of the Debye frequencies from PE-SoS data was performed as described in detail previously.[27,28]

Diffuse reflectance (DR) UV-Vis spectroscopy

Since the materials in this work are air- and/or moisture-sensitive, airtight cells were used for all samples in UV-Vis experiments in order to measure reliable optical bandgap values. Sample powders were spread on the $BaSO_4$ powder standard inside an Ar- or N_2-filled glovebox. DR spectra were recorded using a Shimadzu, UV-2600 UV-Vis spectrophotometer within a wavelength range of 190–1300 nm.

Computational details

Corresponding calculations were performed in the framework of DFT within the Generalised Gradient Approximation (GGA), using the Perdew–Burke–Ernzerhof (PBE)[35] exchange–correlation functional as implemented in the Vienna *Ab Initio* Simulation Package (VASP).[36,37] In these calculations, the valence electron density was expanded using a plane-wave basis set with kinetic energy cut-offs of 650, 550, and 500 eV for $LiAlCl_4$, $LiAlBr_4$ and $LiAlI_4$, respectively. Energy convergence tests revealed negligible energy variations if the plane-waves basis set was enlarged further. The effect of the core electrons on the valence region was evaluated by the Projector Augmented Wave (PAW) method described by Blöchl and implemented by Kresse and Joubert.[38,39] For each of the structures, the necessary numerical integrations in reciprocal space were realised using a *Γ*-centred Monkhorst–Pack mesh of special *k*-points, with a grid size optimised until convergence below 10^{-3} eV was achieved ($6 \times 6 \times 3$ for each of the halides).[40] The $LiAlX_4$ structures displayed in Fig. 1 were modelled using a monoclinic unit cell (space group $P2_1/c$, no. 14), and fixing the lattice parameters of the unit cells to the experimental values obtained from Rietveld refinement against Powder X-ray Diffraction (PXD) data at room temperature.[6] The atomic positions were optimised using a conjugate-gradient algorithm. The structural optimization of atomic positions within the experimental unit cell was continued until the forces acting on all atoms were smaller than 10^{-3} eV $Å^{-1}$. The threshold convergence for the

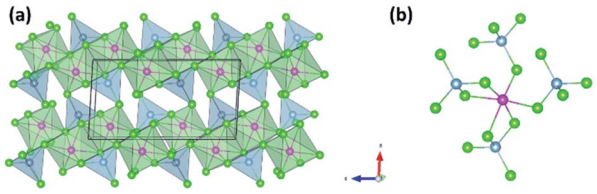

Fig. 1 Optimised (DFT/PBE) crystal structures of $LiAlCl_4$ ($P2_1/c$) projected along the *b*-axis as visualised with VESTA[41] showing: (a) a polyhedral representation of the extended structure and (b) the linkage between an $LiCl_6$ octahedron and neighbouring $AlCl_4$ tetrahedra. Li, Al, and Cl atoms are represented by pink, blue, and green spheres, respectively.

electronic energy was set to 10^{-5} eV. A Gaussian smearing with a smearing width of 0.2 eV was used to enhance the convergence, although the final total energies were always extrapolated to 0 K. All calculations were performed in a non-spin-polarised formalism.

Calculations to predict the phonon spectra were performed by the supercell approach. Real-space force constants of supercells were calculated employing Density Functional Perturbation Theory (DFPT) as implemented in VASP. Phonon frequencies and irreducible representations were calculated from the force constants using the PHONOPY code.[42] For $LiAlX_4$, force constants were computed from a $2 \times 2 \times 1$ supercell expansion with the same k-point sampling for all X. Raman spectra were computed from the above phonon calculations and the respective macroscopic dielectric tensors using the Finite Displacement (FD) method as implemented in VASP.[43,44] Since the Raman active frequency values calculated by these methods are generally underestimated compared to the corresponding experimental frequencies,[45] the former were scaled-up by a factor of 1.02 as suggested by Kesharwani *et al.*[46] The average vibrational frequency, ω_{av}, of the given compound, which is the phonon frequency weighted by the Vibrational Density of States (VDOS), was estimated using eqn (4) and is denoted here as the phonon band centre, representing the average phonon energy:[32]

$$\omega_{av} = \frac{\int \omega \mathrm{VDOS}(\omega) \mathrm{d}\omega}{\int \mathrm{VDOS}(\omega) \mathrm{d}\omega} \quad (4)$$

The phonon band centre can be viewed as the centroid of the VDOS. By replacing VDOS(ω) by the total VDOS or by one of the atom-projected VDOS (for instance, the Li-projected VDOS), one can obtain the total phonon band centre or the individual atom phonon band centre (*i.e.* lithium in this case), respectively.

Results and discussion

Electronic structure

A good SSE must possess, among other properties, a high ionic conductivity and low electronic conductivity, *i.e.* it should be an electronic insulator (with a wide band gap). In this work, electronic structure calculations were conducted to predict and analyse the band gap energies (E_g) in $LiAlX_4$ (X = Cl, Br, I), which have been shown to correlate with the electrochemical oxidative stability of SSEs, and to study the nature of interaction between Li^+ and complex $[AlX_4]^-$ ions.[47] However, it is important to underscore that although a large band gap is a necessary criterion, it alone cannot guarantee the compatibility of a SSE with a high-voltage cathode (which is determined by the SSE oxidation potential).[48] This is because the band edges of the SSE must be positioned relative to those of the cathode so as to prevent electron transfer to the latter.[49,50] The DFT calculations, carried out by single-point calculations with the PBE-optimized structure show that each of the $LiAlX_4$ materials exhibits a wide indirect band gap along the $\Gamma \rightarrow Z$ direction, with values of 5.61, 4.36, and 3.44 eV for X = Cl, Br, and I, respectively (see Fig. 2a; ESI, S2 and S3†). Nevertheless, it should be noted that direct transitions at Γ point are just ~0.03 eV higher than the indirect ones. Since both transitions are very similar in energy, it is expected that the experimental optical behaviour will be dominated by the direct transition since such transitions are not phonon-assisted and thus have a greater probability to occur. It also worth noting that the PBE functional is known to underestimate the band gap and, hence, the values above can be considered as the lower bounds. As expected, the contribution to the covalency of the bonding between Li^+ and the complex $[AlX_4]^-$ anions increases from Cl < Br < I, which is characterised by a decrease (in absolute values) in the anion p-band centres with respect to the mid-gap (Fig. 2b; ESI, S4†).[47] The covalency of the bonds was found to correlate with the oxidative potential limit (as determined from Linear Sweep Voltammetry; LSV.[6] ESI, Fig. S19†). This correlation is consistent with the observation that the measured oxidative potential increases with the band gap width (see Fig. 4a; ESI, S5†).[47] At this point it is also worth noting the consistency between the oxidative potential limits for both solid $LiAlCl_4$ and $LiAlBr_4$ (4.4 V and 3.4 V *vs.* Li^+/Li, respectively)[6] and the corresponding $[AlCl_4]^-$ and $[AlBr_4]^-$ anions (onsets *ca.* 4.4 V and 3.5 V *vs.* Li^+/Li, respectively) in liquid electrolytes (1 M EC/DMC 1 : 1).[51] Since the metals remain the same in each halide, *i.e.* Li and Al, then the band gap will be dependent only on the position of the halide anion valence p-band edges. Diffuse Reflectance UV-Vis spectroscopy (DR-UV-Vis) measurements were performed to obtain experimental values for the optical band gaps, allowing us to make

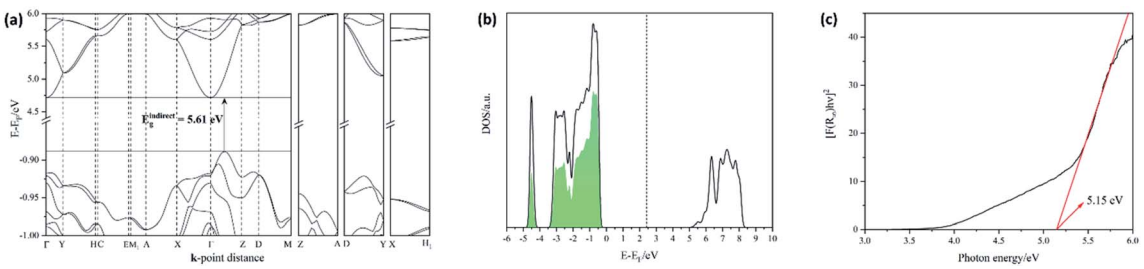

Fig. 2 (a) Computed (DFT/PBE) band structures of $LiAlCl_4$, with band energies scaled to the Fermi level (E_F). High symmetry k-points are noted as well as the indirect gap region between the VBM and the CBM. (b) Example of Cl-projected electronic DOS in $LiAlCl_4$. The Cl p-band centre was computed by integrating over the occupied states closer to the VBM (green area) with respect to the mid-gap energy indicated by a dashed line. (c) Tauc plot for allowed direct transitions in $LiAlCl_4$. The red line corresponds to the linear fit.

comparisons with our calculated data. The DR-UV-Vis spectra of the three lithium tetrahaloaluminates (ESI, Fig. S6†) show that these materials have absorption edges located in the near- and mid-UV regions. Tauc plots to fit allowed direct transitions to the data yielded measured band gaps of 5.15, 4.01 and 3.01 eV for X = Cl, Br, and I, respectively (Fig. 2c; ESI, S7†), in relatively good agreement with the computed values (despite using a GGA functional) and confirming the premise that all three lithium tetrahaloaluminates are electronic insulators. The electrochemical windows for $LiAlX_4$ have been previously calculated in the literature for X = Cl and Br yielding values of 2.8 V and 2.1 V (*vs.* Li^+/Li, respectively).[52] If these computed values are plotted against the measured optical band gaps (ESI, Fig. S8†) then following the assumption that the two quantities are related linearly, one can extrapolate to predict an Electrochemical stability Window (EW) of approximately 1.4 V *vs.* Li^+/Li for $LiAlI_4$.

Vibrational density of states

Recent work has demonstrated the correlation between lattice dynamics, as manifested by the phonon band centre (eqn (4)), with select and important properties of ionic conductors such as the enthalpy of migration and the electrochemical oxidative stability.[32] Experimentally, the VDOS can be obtained *via* INS measurements. Since the neutron scattering lengths and, hence, coherent cross sections are different for different elements, the VDOS derived from simulations need to be neutron-weighted before valid comparisons between computed and measured VDOS can be made.[53] Fig. 3 shows the computed phonon dispersions and neutron-weighted zero-temperature harmonic VDOS, respectively, for $LiAlCl_4$ (results for the bromide and iodide analogues are shown in the ESI, Fig. S9 and 10†).

INS spectra were measured at 10 K as an experimental verification of the calculated VDOS results and to assess the accuracy of the phonon calculations. This was an important test since the latter form a key component towards understanding the structure–property relationships in $LiAlX_4$ materials. It was found that the experimental spectrum at 10 K and computed VDOS (0 K) are in close qualitative agreement. It is noticeable that the spectral resolution achieved for $LiAlBr_4$ and $LiAlI_4$ decreased significantly as compared to the chloride due to the lower neutron scattering cross sections of both Br (5.9 barn) and I (3.81 barn) *vs.* Cl (16.8 barn). In all cases, the systems were found to be vibrationally, *i.e.* dynamically, stable. Substitution of lighter halides for heavier equivalents in isostructural $LiAlX_4$ led to a significant softening of the Li-projected VDOS, which can be quantified as a decrease in the average vibrational frequency, ω_{Li}. The ω_{Li} values for the haloaluminates each lie in the 20–30 meV range (ESI, Table S1†). This softening and corresponding decrease in ω_{Li} can be rationalised by the weaker coulombic (less ionic) interactions between Li^+ and the respective complex $[AlX_4]^-$ ions as Cl is replaced by more polarisable Br and I. There is, therefore, a direct correlation between the Li phonon band centre and the anion-p band centres in the respective electronic DOS. (ESI, Fig. S11†). The

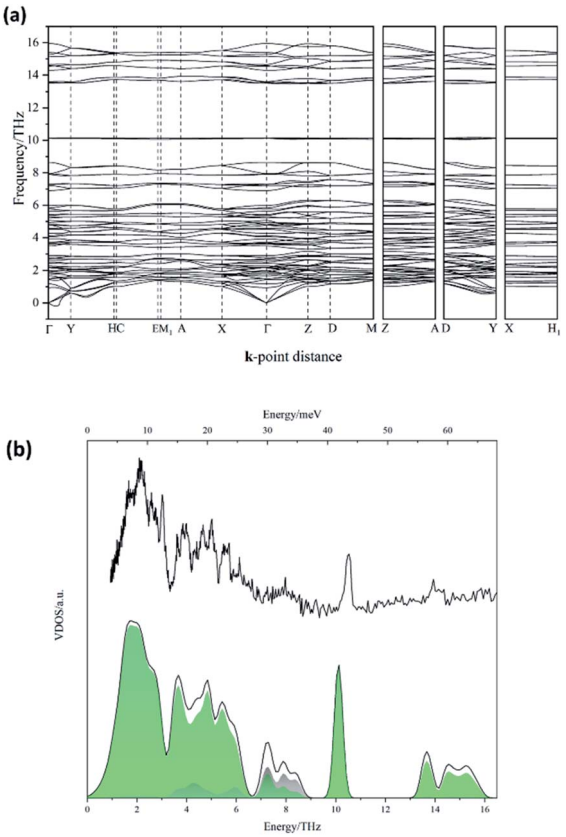

Fig. 3 (a) Computed (DFPT/PBE) phonon dispersion curves of $LiAlCl_4$. (b) Comparison of the computed (DFPT/PBE – bottom) neutron-weighted VDOS *vs.* the measured INS spectrum collected at 10 K for $LiAlCl_4$ (TOSCA, ISIS – top). Cl-VDOS and Li-VDOS are shown in green and grey, respectively, superimposed over the total VDOS.

softening of the Li-projected VDOS also correlates with a decrease in the measured activation energies (Fig. 4b), as previously reported for different families of Li^+ and Na^+ ionic conductors.[31,32,47] The above observations support the hypothesis that softer lattices allow larger displacement amplitudes (u) of the mobile ion (Li^+), which are associated with low phonon frequencies (ω_E) in the Einstein model:

$$\left\langle |u|^2 \right\rangle = \frac{3k_B T}{m\omega_E{}^2} \quad (5)$$

where k_B, T, and m are the Boltzmann constant, absolute temperature, and mass of the mobile species, respectively. Conversely, the average vibrational frequencies (phonon band centres) of the respective halides, ω_X, were found to correlate with the oxidative potential limit, *i.e.* lowering ω_X causes a decrease in the stability of $LiAlX_4$ towards electrochemical oxidation (Fig. 4c). Muy *et al.*[32] argued that this correlation might be kinetic in origin, since lowering ω_X implies a softer and more mobile anion sublattice, which in turn decreases the kinetic barrier for the oxidation reactions. In addition, our current work validates the premise that the acoustic phonons become softer when increasing the anion framework

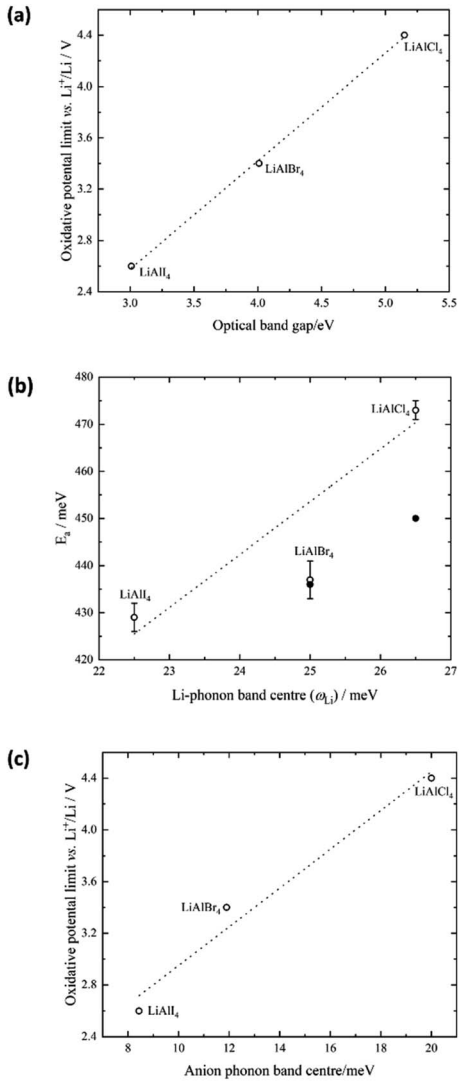

Fig. 4 (a) Correlation between the measured oxidative potential limit (from Linear Sweep Voltammetry; LSV)[6] and the measured direct optical band gap (from DR-UV-Vis data) of $LiAlX_4$ (X = Cl, Br, I) materials. The dotted line corresponds to a linear fit ($R^2 = 1.00$). (b) Correlation between Li^+ migration activation energies as measured *via* ^7Li solid state NMR[54] (solid circles) and electrochemical impedance spectroscopy (EIS) techniques[6,55] (open circles) and the computed (DFPT/PBE) Li phonon band centre (ω_{Li}) for $LiAlX_4$ (X = Cl, Br, I). The dotted black line corresponds to a linear fit to the EIS data ($R^2 = 0.885$). (c) Correlation between the oxidative potential limit (as measured by LSV[6]) and the computed (DFPT/PBE) anion phonon band centre (ω_X) for $LiAlX_4$ (X = Cl, Br, I). The dotted line corresponds to a linear fit ($R^2 = 0.974$).

polarisability (ESI, Fig. S12†), in agreement with previous experimental observations in Li^+ and Na^+ ionic conductors.[27,28]

Raman spectra

Raman spectra were measured for the $LiAlX_4$ materials for comparison with the INS spectra and information regarding the vibrational modes of complex anionic species such as $[AlX_4]^-$ can be readily found in the literature; however, these data

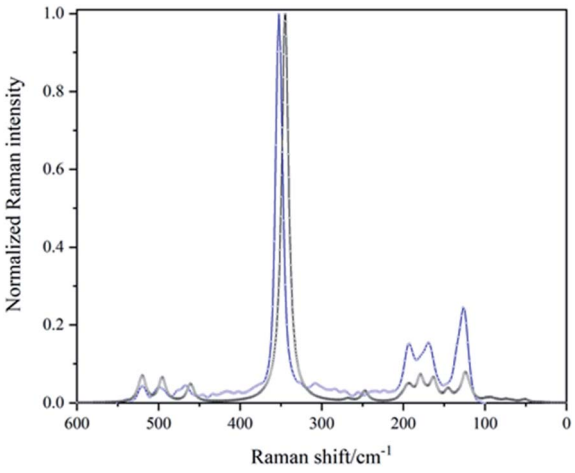

Fig. 5 Computationally simulated (DFT/FD/PBE; black line) *vs.* experimentally observed (blue line) Raman spectra for $LiAlCl_4$ ($\lambda_{laser} = 1064$ nm).

correspond to the gas phase species rather than solid state compounds and do not consider the myriad of ionic interactions in a crystalline system.[51,54] Corresponding calculations for solid-state systems can therefore make an important contribution to the understanding and unbiased assignment of the experimental spectra, especially as new materials are synthesised. $LiAlX_4$ (X = Cl, Br, I) crystallize in monoclinic space group $P2_1/c$ (C_{2h}^5) with twenty-four atoms per unit cell. Therefore, seventy-two phonon modes of vibration are expected (three acoustic and sixty-nine optical modes).

According to a nuclear site analysis (see ESI†),[56] the optical modes at the Γ point are as follows:

$$\Gamma_{optic} = 18A_g\,(R) + 17A_u\,(IR) + 18B_g\,(R) + 16B_u\,(IR),$$

where R and IR refer to the allowed Raman and infrared modes, respectively. The Raman bands and frequencies generated by the FD method are summarised in the ESI (Table S6†). Although 36 Raman active modes are predicted for the $LiAlX_4$ materials, some of these bands were found to exhibit very low intensity and, thus, cannot be easily observed experimentally (Fig. 5; ESI, S13–S15†).

Generally, there is good agreement between the measured and calculated Raman spectra within the harmonic approximation. However, the assignment of the vibrational modes to the experimental data is not always straightforward, since some of the observed bands appear as a convolution of two individual modes, *e.g.* the experimentally observed bands at 499, 406, and 343 cm^{-1} for $LiAlCl_4$, $LiAlBr_4$ and $LiAlI_4$, respectively, are a convolution of B_g and A_g modes. It is worth noting that Raman active vibrations that might have been attributed to starting materials in the synthesis process such as AlX_3 were not present in the respective experimental Raman spectra (ESI, Fig. S16†). This supports evidence from diffraction (ESI, Fig. S1†) and the findings from previous thermal analysis to confirm the efficacy of the mechanochemical synthesis in yielding high purity final

products.[6] The relevant Raman spectra for the respective AlX_3 materials are also included in the ESI for reference in Fig. S17 and Table S7.†

Correlation between lattice dynamics and ionic transport: the Meyer–Neldel rule

Fig. 6a shows the correlation between the two proposed descriptors to quantify the effect of lattice dynamics on the ionic transport, *i.e.* the Debye frequency (ν_D, as obtained from PE-SoS measurements; ESI, Fig. S18†) and the Li phonon band centre (ω_{Li}, taken from the DFPT/PBE calculations). As can be seen, the respective ν_D and ω_{Li} values lie within the same approximate frequency range, with a relationship of $\nu_D \sim 0.5\omega_{Li}$ in $LiAlCl_4$, for example. Despite the fact that the extracted Li phonon band centres are obtained under the zero-temperature harmonic approach, which present inherent limitations as recently highlighted by Cazorla and co-workers,[29] one would at least expect the trend among the halides to remain true at room temperature due to the isostructural nature of the $LiAlX_4$ compounds.

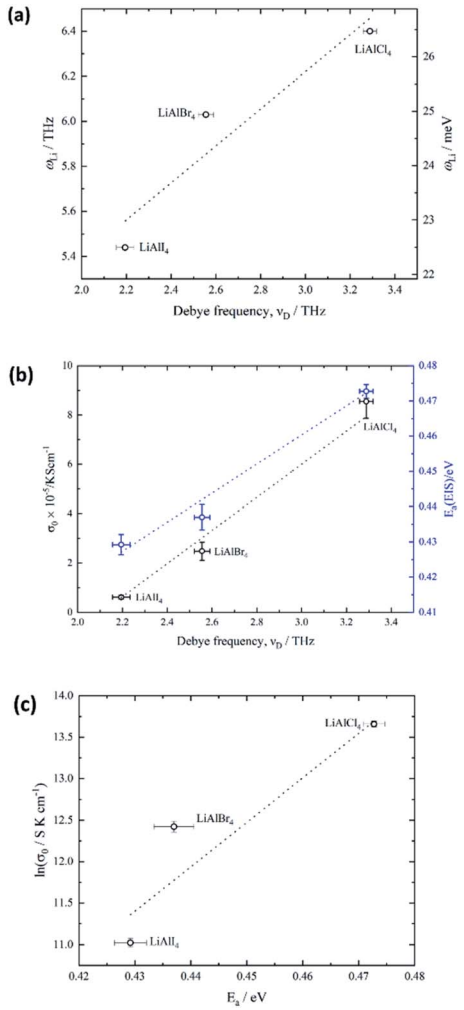

Fig. 6 (a) Correlation between the extracted Debye frequencies from PE-SoS measurements and the computed (DFPT/PBE) Li phonon band centres for $LiAlX_4$ materials (X = Cl, Br, I). The dotted line corresponds to a linear fit ($R^2 = 0.898$); (b) correlation between the extracted Debye frequencies (from PE-SoS measurements) and the extracted pre-factors and activation energies (from EIS measurement) in $LiAlX_4$ materials (X = Cl, Br, I).[6] The dotted lines correspond to linear fits (blue, $R^2 = 0.987$) (black, $R^2 = 0.981$). (c) Natural logarithm of the Arrhenius pre-factor *vs.* the respective activation energies obtained from EIS measurements for $LiAlX_4$ materials (X = Cl, Br, I). The dotted line corresponds to the linear fit provided by applying the Meyer–Neldel rule ($R^2 = 0.922$).

Traditionally, it is usually expected that a highly polarisable anion framework is required to achieve high ionic conductivity in the solid state.[22] A common interpretation of this statement is that replacing harder anions (*e.g.* O^{2-}) with softer equivalents (*e.g.* S^{2-}) within the same structural family (where similar conduction mechanisms would be inferred to prevail), would increase the ionic conductivity (σ) *via* a decrease in E_a, the activation energy for the migration of the mobile cation (eqn (2)). However, there is no such straightforward relationship between σ and E_a for the haloaluminates, since the room temperature ionic conductivity first slightly increases but then subsequently decreases when switching from X = Cl through Br to I. The implication is that the role of the pre-exponential term across the halide series is by no means insignificant and similar behaviour has been reported previously for lithium argyrodites[27] and sodium thiophosphates.[28] At the root of this apparent non-compliance by the haloaluminates is that both σ_0 and E_a in eqn (2) decrease simultaneously when the anion becomes more polarizable (quantified in terms of either ν_D or ω_{Li} as shown in Fig. 6b, for example). Thus, there is an optimum value of the pre-exponential and exponential factors that maximises σ, a phenomenon first described by Meyer and Neldel in their study of carrier transport in semiconductor oxides.[57] By taking the expression of the pre-exponential factor (eqn (3)), it can be seen that, since γ (geometric factor), c (carrier density), Z (charge number of the mobile ion), and e (the elementary charge) are inferred to be constant in $LiAlX_4$, the above equation leaves only three variables, *i.e.* the attempt frequency (ν_0), jump distance (a_0), and the entropy of migration (ΔS_m). Under the assumption that $\nu_0 \approx \nu_D$, the decrease in ν_0 it is not enough in itself to explain the decrease in σ_0 (Fig. 6b) with halide, X. This relationship must be predominantly governed by ΔS_m (since the jump distance between adjacent sites, a_0, increases from Cl through Br to I, as the lattice parameters increase).[6,30,58] According to the Meyer–Neldel rule (MNR; also known as the compensation rule), there is a linear relationship between $\ln(\sigma_0)$ and E_a in the form of

$$\ln \sigma_0 = \alpha E_a + \beta, \tag{6}$$

where α and β are positive constants for a given series of compounds, and the reciprocal of α is termed as the Meyer–Neldel energy, Δ_0. Thus, by combining eqn (2) and (6):

$$\sigma = \frac{1}{T}\exp\left[E_a\left(\frac{1}{\Delta_0} - \frac{1}{k_B T}\right) + \beta\right] \tag{7}$$

Based on eqn (7), Gao *et al.*[59] highlighted that the relationship between σ and E_a depends on the sign of $(1/\Delta_0 - 1/k_B T)$ at a given temperature. For example, for materials where $\Delta_0 > k_B T$ (labelled

as type 1), decreasing E_a would lead to a higher σ. Conversely, if $\Delta_0 < k_BT$, increasing E_a would lead to a higher σ (type 2). On the other hand, for materials where $\Delta_0 \sim k_BT$, σ is not sensitive to changes in E_a (type 3). A similar behaviour has been derived for proton conductors, where the relationship between σ and E_a depends on the sign of $(1/T_{iso} - 1/T)$, where T_{iso} is termed the isokinetic temperature.[60] Although the fit across the halide series deviates from linearity (Fig. 6c, $R^2 = 0.922$) one can obtain a tentative value for Δ_0 of 19(5) meV, which lies within the energy scale of the Li-phonon band centres obtained from DFT (Fig. 4b, ESI Table S6†). Based on the value of Δ_0, it is not surprising that σ_{RT} remains in the range 0.012–0.033 mS cm^{-1} despite the decrease in E_a when switching from X = Cl through Br to I, since $k_BT \sim 26$ meV at 298 K. The above results support the idea that the Meyer–Neldel energy can be explained by the Multi-Excitation Entropy (MEE) proposed by Yelon *et al.*[61] Within this framework, for any thermally activated process, the activation entropy (ΔS_m in eqn (1)) is proportional to the E_a by taking Δ_0 as the average energy of the phonons in the system. ΔS_m arises from the multiplicity of microstates, from a statistical mechanics point of view, associated with the absorption of excitations, *i.e.* phonons, needed to overcome a migration barrier E_a.[58] In this regard, our results verify that the interplay between σ and E_a depends on the relative magnitude of Δ_0 and k_BT, and that Δ_0 can be linked to the average energy of the phonons, *i.e.* ω_{Li}, in ionic conductors that obey the Meyer–Neldel rule.[58,59]

Conclusions

In this work we studied the effect of lattice polarisability on the ionic conductivity and the electrochemical oxidative stability of lithium tetrahaloaluminates, based on lattice dynamics and electronic structure considerations. Our results demonstrate that the activation energy for Li^+ diffusion in $LiAlX_4$ (X = Cl, Br, I) correlates with the two proposed descriptors that quantify the overall lattice vibrations in solids, *i.e.* the Debye frequency and the Li-phonon band centre, and that both quantities lie within the same approximate frequency range. We also show that the oxidative potential limit correlates with the X^- phonon band centre, and that the EW and optical band gap are interlinked, which points to the possibility of estimating the upper limit of the EW by DR-UV-Vis. Nevertheless, that ω_{Li} and ω_X are obtained from calculations rather than by experiment, places limitations on an interpretation of lattice dynamics from INS data. Furthermore, for materials containing elements with low neutron scattering cross sections, long scans are essential to achieve good spectral resolution. In addition, further experimental and computational tools are needed in order to determine migration entropies in SSEs accurately. Finally, our data show that softer lattices provide lower activation energies for Li^+ migration in isostructural compounds (where the conduction pathways are known not to change significantly). However, this work illustrates once again that an improvement in ionic conductivity does not automatically follow since E_a and σ_0 correlate in line with expectations emergent from the Meyer–Neldel rule. Preliminary results indicate that the anion sublattice polarisability could be tuned even further by judicious substitution and the results of these studies will be communicated in due course.

Conflicts of interest

There are no conflicts to declare

Acknowledgements

The authors acknowledge the Advanced Human Capital Program of the National Commission for Scientific and Technological Research (CONICYT/Becas Chile/No. 72170338) for a PhD scholarship for N. F. G., the Royal Society of Chemistry for a Researcher Mobility Grant No. RM1602-2758 and the EPSRC for associated funding under grant EP/N001982/1. The authors also thank the UK Science and Technology Facilities Council (STFC) for the award of neutron beamtime on TOSCA spectrometer at the ISIS Facility *via* the direct access route. N. M. and W. Z. are grateful for support by the Deutsche Forschungsgemeinschaft (DFG)under grant number ZE 1010/4-1. M. L., F. V., and F. I. thank the Spanish MCIN/AEI/10.13039/501100011033 funded RTI2018-095460 B-I00 and María de Maeztu MDM-2017-0767 grants, including funding from European Union and, in part, by and COST Action CA18234. Finally, M. L. thanks Universitat de Barcelona for an APIF predoctoral contract.

References

1 J. C. Bachman, S. Muy, A. Grimaud, H.-H. Chang, N. Pour, S. F. Lux, O. Paschos, F. Maglia, S. Lupart, P. Lamp, L. Giordano and Y. Shao-Horn, *Chem. Rev.*, 2016, **116**, 140–162.
2 J. Janek and W. G. Zeier, *Nat. Energy*, 2016, **1**, 16141.
3 Y. Kato, S. Hori, T. Saito, K. Suzuki, M. Hirayama, A. Mitsui, M. Yonemura, H. Iba and R. Kanno, *Nat. Energy*, 2016, **1**, 16030.
4 F. Han, Y. Zhu, X. He, Y. Mo and C. Wang, *Adv. Energy Mater.*, 2016, **6**, 1501590.
5 C. Zheng, J. Zhang, Y. Xia, H. Huang, Y. Gan, C. Liang, X. He, X. Tao and W. Zhang, *Small*, 2021, **17**, 2101326.
6 N. Flores-González, N. Minafra, G. Dewald, H. Reardon, R. I. Smith, S. Adams, W. G. Zeier and D. H. Gregory, *ACS Mater. Lett.*, 2021, **3**, 652–657.
7 J. Liang, X. Li, S. Wang, K. R. Adair, W. Li, Y. Zhao, C. Wang, Y. Hu, L. Zhang, S. Zhao, S. Lu, H. Huang, R. Li, Y. Mo and X. Sun, *J. Am. Chem. Soc.*, 2020, **142**, 7012–7022.
8 L. Zhou, C. Y. Kwok, A. Shyamsunder, Q. Zhang, X. Wu and L. F. Nazar, *Energy Environ. Sci.*, 2020, **13**, 2056–2063.
9 L. Zhou, T.-T. Zuo, C. Y. Kwok, S. Y. Kim, A. Assoud, Q. Zhang, J. Janek and L. F. Nazar, *Nat. Energy*, 2022, **7**, 83–93.
10 H. Kwak, D. Han, J. Lyoo, J. Park, S. H. Jung, Y. Han, G. Kwon, H. Kim, S.-T. Hong, K.-W. Nam and Y. S. Jung, *Adv. Energy Mater.*, 2021, **11**, 2003190.
11 T. Asano, A. Sakai, S. Ouchi, M. Sakaida, A. Miyazaki and S. Hasegawa, *Adv. Mater.*, 2018, **30**, 1803075.
12 R. Schlem, S. Muy, N. Prinz, A. Banik, Y. Shao-Horn, M. Zobel and W. G. Zeier, *Adv. Energy Mater.*, 2020, **10**, 1903719.
13 R. Schlem, T. Bernges, C. Li, M. A. Kraft, N. Minafra and W. G. Zeier, *ACS Appl. Energy Mater.*, 2020, **3**, 3684–3691.

14 S. Wang, Q. Bai, A. M. Nolan, Y. Liu, S. Gong, Q. Sun and Y. Mo, *Angew. Chem., Int. Ed.*, 2019, **58**, 8039–8043.
15 X. Li, J. Liang, N. Chen, J. Luo, K. R. Adair, C. Wang, M. N. Banis, T.-K. Sham, L. Zhang, S. Zhao, S. Lu, H. Huang, R. Li and X. Sun, *Angew. Chem., Int. Ed.*, 2019, **58**, 16427–16432.
16 Z. Xu, X. Chen, K. Liu, R. Chen, X. Zeng and H. Zhu, *Chem. Mater.*, 2019, **31**, 7425–7433.
17 Y. Liu, S. Wang, A. M. Nolan, C. Ling and Y. Mo, *Adv. Energy Mater.*, 2020, **10**, 2002356.
18 K.-H. Park, K. Kaup, A. Assoud, Q. Zhang, X. Wu and L. F. Nazar, *ACS Energy Lett.*, 2020, **5**, 533–539.
19 K. Wang, Q. Ren, Z. Gu, C. Duan, J. Wang, F. Zhu, Y. Fu, J. Hao, J. Zhu, L. He, C.-W. Wang, Y. Lu, J. Ma and C. Ma, *Nat. Commun.*, 2021, **12**, 4410.
20 S. Ohno, A. Banik, G. F. Dewald, M. A. Kraft, T. Krauskopf, N. Minafra, P. Till, M. Weiss and W. G. Zeier, *Prog. Energy*, 2020, **2**, 022001.
21 J. B. Goodenough, in *Solid State Electrochemistry*, ed. P. G. Bruce, Cambridge University Press, Cambridge, 1994, p. 55.
22 A. R. West, *Solid State Chemistry and its Applications*, Wiley, 2014.
23 P. P. Kumar and S. Yashonath, *J. Chem. Sci.*, 2006, **118**, 135–154.
24 Z. Zhang, Y. Shao, B. Lotsch, Y.-S. Hu, H. Li, J. Janek, L. F. Nazar, C.-W. Nan, J. Maier, M. Armand and L. Chen, *Energy Environ. Sci.*, 2018, **11**, 1945–1976.
25 T. Famprikis, P. Canepa, J. A. Dawson, M. S. Islam and C. Masquelier, *Nat. Mater.*, 2019, **18**, 1278–1291.
26 Y. Wang, W. D. Richards, S. P. Ong, L. J. Miara, J. C. Kim, Y. Mo and G. Ceder, *Nat. Mater.*, 2015, **14**, 1026–1031.
27 M. A. Kraft, S. P. Culver, M. Calderon, F. Böcher, T. Krauskopf, A. Senyshyn, C. Dietrich, A. Zevalkink, J. Janek and W. G. Zeier, *J. Am. Chem. Soc.*, 2017, **139**, 10909–10918.
28 T. Krauskopf, C. Pompe, M. A. Kraft and W. G. Zeier, *Chem. Mater.*, 2017, **29**, 8859–8869.
29 A. K. Sagotra, D. Chu and C. Cazorla, *Phys. Rev. Mat.*, 2019, **3**, 035405.
30 S. Duan, C. Huang, M. Liu, Z. Cao, X. Tian, S. Hou, J. Li, B. Huang and H. Jin, *J. Mat. Chem. A*, 2021, **9**, 7817–7825.
31 T. Krauskopf, S. Muy, S. P. Culver, S. Ohno, O. Delaire, Y. Shao-Horn and W. G. Zeier, *J. Am. Chem. Soc.*, 2018, **140**, 14464–14473.
32 S. Muy, J. C. Bachman, L. Giordano, H.-H. Chang, D. L. Abernathy, D. Bansal, O. Delaire, S. Hori, R. Kanno, F. Maglia, S. Lupart, P. Lamp and Y. Shao-Horn, *Energy Environ. Sci.*, 2018, **11**, 850–859.
33 R. S. Pinna, M. Zanetti, S. Rudić, S. F. Parker, J. Armstrong, S. P. Waller, D. Zacek, C. Smith, S. M. Harrison, G. Gorini and F. Fernandez-Alonso, *J. Phys. Conf. Ser.*, 2018, **1021**, 012029.
34 J. Taylor, O. Arnold, J. Bilheaux, A. Buts, S. Campbell, M. Doucet, N. Draper, R. Fowler, M. Gigg, V. Lynch, A. Markvardsen, K. Palmen, P. Parker, P. Peterson, S. Ren, M. Reuter, A. Savici, R. Taylor, R. Tolchenov, R. Whitley, W. Zhou and J. Zikovsky, *presented in part at the APS March Meeting Abstracts*, February 01, 2012.
35 J. P. Perdew, K. Burke and M. Ernzerhof, *Phys. Rev. Lett.*, 1996, **77**, 3865–3868.
36 G. Kresse and J. Furthmüller, *Phys. Rev. B: Condens. Matter Mater. Phys.*, 1996, **54**, 11169–11186.
37 G. Kresse and J. Furthmüller, *Comput. Mater. Sci.*, 1996, **6**, 15–50.
38 P. E. Blöchl, *Phys. Rev. B: Condens. Matter Mater. Phys.*, 1994, **50**, 17953–17979.
39 G. Kresse and D. Joubert, *Phys. Rev. B: Condens. Matter Mater. Phys.*, 1999, **59**, 1758–1775.
40 H. J. Monkhorst and J. D. Pack, *Phys. Rev. B: Condens. Matter Mater. Phys.*, 1976, **13**, 5188–5192.
41 K. Momma and F. Izumi, *J. Appl. Crystallogr.*, 2011, **44**, 1272–1276.
42 A. Togo and I. Tanaka, *Scripta Mater.*, 2015, **108**, 1–5.
43 D. Porezag and M. R. Pederson, *Phys. Rev. B: Condens. Matter Mater. Phys.*, 1996, **54**, 7830–7836.
44 A. Fonari and S. Stauffer, 2013, **https://github.com/raman-sc/VASP/**.
45 P. Vajeeston, P. Ravindran and H. Fjellvåg, *J. Phys. Chem. A*, 2011, **115**, 10708–10719.
46 M. K. Kesharwani, B. Brauer and J. M. L. Martin, *J. Phys. Chem. A*, 2015, **119**, 1701–1714.
47 S. Muy, J. Voss, R. Schlem, R. Koerver, S. J. Sedlmaier, F. Maglia, P. Lamp, W. G. Zeier and Y. Shao-Horn, *iScience*, 2019, **16**, 270–282.
48 T. K. Schwietert, V. A. Arszelewska, C. Wang, C. Yu, A. Vasileiadis, N. J. J. de Klerk, J. Hageman, T. Hupfer, I. Kerkamm, Y. Xu, E. van der Maas, E. M. Kelder, S. Ganapathy and M. Wagemaker, *Nat. Mater.*, 2020, **19**, 428–435.
49 P. Peljo and H. H. Girault, *Energy Environ. Sci.*, 2018, **11**, 2306–2309.
50 T. Thompson, S. Yu, L. Williams, R. D. Schmidt, R. Garcia-Mendez, J. Wolfenstine, J. L. Allen, E. Kioupakis, D. J. Siegel and J. Sakamoto, *ACS Energy Lett.*, 2017, **2**, 462–468.
51 F. Scholz, W. Unkrig, P. Eiden, M. A. Schmidt, A. Garsuch and I. Krossing, *Eur. J. Inorg. Chem.*, 2015, **2015**, 3128–3138.
52 W. D. Richards, L. J. Miara, Y. Wang, J. C. Kim and G. Ceder, *Chem. Mater.*, 2016, **28**, 266–273.
53 D. Bansal, J. Hong, C. W. Li, A. F. May, W. Porter, M. Y. Hu, D. L. Abernathy and O. Delaire, *Phys. Rev. B: Condens. Matter Mater. Phys.*, 2016, **94**, 054307.
54 K. Nakamoto, *Infrared and Raman Spectra of Inorganic and Coordination Compounds, Two Volume Set*, Wiley, 2008.
55 K. Yamada, M. Kinoshita, K. Hosokawa and T. Okuda, *Bull. Chem. Soc. Jpn.*, 1993, **66**, 1317–1322.
56 D. L. Rousseau, R. P. Bauman and S. P. S. Porto, *J. Raman Spectrosc.*, 1981, **10**, 253–290.
57 W. Meyer and H. Neldel, *Z. Tech. Phys.*, 1937, **12**, 588–593.
58 S. Muy, R. Schlem, Y. Shao-Horn and W. G. Zeier, *Adv. Energy Mater.*, 2021, **11**, 2002787.
59 Y. Gao, N. Li, Y. Wu, W. Yang and S.-H. Bo, *Adv. Energy Mater.*, 2021, **11**, 2100325.
60 P. Du, N. Li, X. Ling, Z. Fan, A. Braun, W. Yang, Q. Chen and A. Yelon, *Adv. Energy Mater.*, 2022, **12**, 2102939.
61 A. Yelon, B. Movaghar and H. M. Branz, *Phys. Rev. B: Condens. Matter Mater. Phys.*, 1992, **46**, 12244–12250.